



Facile growth of compositionally tuned copper vanadate nanostructured thin films for efficient photoelectrochemical water splitting

Shankara S. Kalanur^a, Hyungtak Seo^{a,b,*}

^a Department of Materials Science and Engineering, Ajou University, Suwon 443-739, Republic of Korea

^b Department of Energy Systems Research, Ajou University, Suwon 443-739, Republic of Korea

ARTICLE INFO

Keywords:

Copper vanadate
Nanorod
Nanoplate
Photoelectrochemical water splitting
Band edge

ABSTRACT

Copper vanadates are considered as one of the most promising photoanode materials for photoelectrochemical (PEC) water splitting owing to their narrow bandgap, stoichiometry-dependent optical and electrical properties, and high stability. However, for technological applications, it is imperative to develop stoichiometrically and structurally tuned copper vanadates for improved performance. In this study, we developed a facile and one-step hydrothermal method for the synthesis of $\text{Cu}_2\text{V}_2\text{O}_7$ nanoplates, $\text{Cu}_5\text{V}_2\text{O}_{10}$ nanorods, and $\text{Cu}_{11}\text{V}_6\text{O}_{26}$ micropillars on a fluorine-doped tin oxide substrate without using a seed layer. The presence of urea during the hydrothermal synthesis significantly affected the film formation and morphology of the copper vanadates. The crystallographic, chemical, and electrochemical properties of the synthesized copper vanadates were investigated. The optimized $\text{Cu}_2\text{V}_2\text{O}_7$, $\text{Cu}_5\text{V}_2\text{O}_{10}$, and $\text{Cu}_{11}\text{V}_6\text{O}_{26}$ electrodes exhibited the highest photocurrent densities of ~ 0.41 , 0.27 , and 0.076 mA cm^{-2} (at 1.23 V vs. reversible hydrogen electrode under 1-sun illumination) and incident photon to current efficiency values of $\sim 24\%$, 18% , and 7.5% (at 300 nm), respectively. The band edge positions of $\text{Cu}_2\text{V}_2\text{O}_7$, $\text{Cu}_5\text{V}_2\text{O}_{10}$, and $\text{Cu}_{11}\text{V}_6\text{O}_{26}$ were estimated on the basis of the spectroscopic and electrochemical results. The synthesis scheme and valuable insights provided in this work can be used for the development of chemically and morphologically optimized copper vanadates for efficient PEC water splitting.

1. Introduction

The development of a novel, sustainable, and clean energy alternatives to fossil fuels is urgently required to prevent environmental degradation [1,2]. Hydrogen as a fuel is considered as an ideal future energy carrier having the potential to replace the depleting fossil fuels [3,4]. Furthermore, as a clean and renewable energy carrier, it could fulfill the global energy demands and mitigate the environmental deterioration [5]. Hence, enormous research efforts in science and engineering have been undertaking to develop a clean and sustainable route to efficiently produce hydrogen using renewable resources [6–8]. Among the various available technologies, the photoelectrochemical (PEC) water splitting using renewable resources such as solar energy and water is considered as the most suitable, environmentally benign, and sustainable approach [9,10]. The successful demonstration of PEC water splitting by Fujishima and Honda in 1972 [10,11] has initiated great research to explore and develop an efficient material for PEC water splitting. However, achieving efficient PEC water splitting using semiconductors is challenging.

During the PEC water splitting, the oxygen evolution reaction (OER)

undergoes on the surface of photoanode material that involves four-electron and multi-proton transfer process. Hence, the properties of photoanode material are highly significant as the photo-assisted OER is kinetically sluggish, due to the multi-processes [12]. The semiconductor photoanode materials are known to be the key components in PEC water splitting systems due to their optical and electrical properties [13–15]. In particular, metal oxide semiconductors have received significant attention as a photoanode material in PEC water splitting because of their favorable band edge positions, a wide range of bandgaps, low cost, and stability during photo-electrolysis [13,16]. The selection criteria for suitable materials for efficient PEC water splitting are as follows: appropriate band edge position (the photo-oxidation and photo-reduction potential of water should lie between the valence and conduction band edge potential of the semiconductor, respectively) and narrow bandgap to absorb significant amount of visible light and stability during the PEC water splitting reaction. However, most of the metal oxide semiconductors do not satisfy all the above-mentioned necessary conditions of PEC water splitting. For example, photoanode materials such as TiO_2 [17], WO_3 [1,18], and ZnO [19] absorb a very small range of incident solar light (visible light), which limits their PEC

* Corresponding author at: Department of Materials Science and Engineering, Ajou University, Suwon 443-739, Republic of Korea.

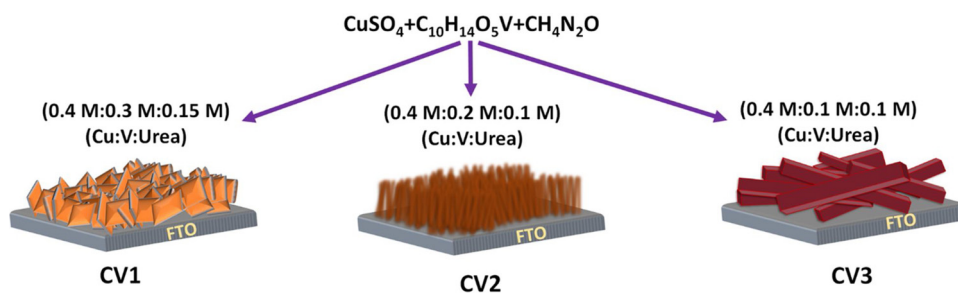
E-mail address: hseo@ajou.ac.kr (H. Seo).

<https://doi.org/10.1016/j.apcatb.2019.02.069>

Received 21 November 2018; Received in revised form 20 February 2019; Accepted 24 February 2019

Available online 26 February 2019

0926-3373/ © 2019 Elsevier B.V. All rights reserved.



Scheme 1. The optimized synthesis condition of CV1, CV2 and CV3 thin films on FTO.

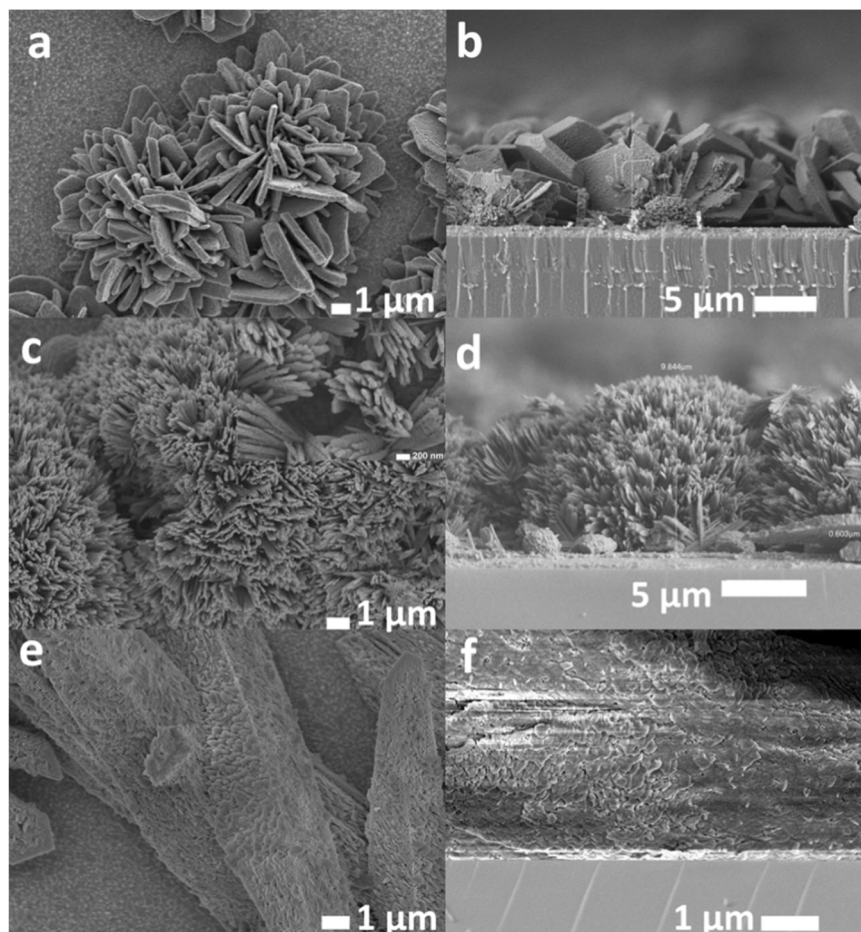


Fig. 1. Surface (a), (c), (e) and cross-sectional (b), (d), (f) SEM images of the CV1, CV2, and CV3 thin films on FTO, respectively. Inset in (c) shows the magnified image of CV2.

activity. Materials such as Fe_2O_3 [20] suffer from poor electronic properties. On the other hand, despite having a suitable bandgap and well-matched band edge positions, Cu_2O [21,22] shows poor PEC water splitting performance owing to its poor stability. This indicates that the binary oxide materials (single junction photoanodes such as TiO_2 , WO_3 , Fe_2O_3 , Cu_2O , etc.), face various limitations that affect their PEC water splitting activity. To overcome the various limitations of metal oxides, different binary oxides were mixed to form ternary metal oxides which are free from the shortcomings shown by the binary metal oxides. The literature reports a variety of ternary metal oxides such as BiVO_4 [23], ZnFe_2O_4 [24,25], CuWO_4 [26], and $\text{Cu}_2\text{V}_2\text{O}_7$ [27], which have been extensively studied for PEC water splitting [28].

Recently, copper vanadate materials have gained immense attention as a photoanode material in PEC water splitting owing to their excellent optical and electrical properties [29]. Copper vanadates are n-type materials having an indirect band gap of $\sim 2\text{ eV}$, that allows significant

absorption of sunlight for the efficient PEC water splitting. Furthermore, the copper vanadates are highly stable in aqueous PEC conditions. Interestingly, copper vanadates exist in numerous stable phases having various Cu:V stoichiometric ratios. Several copper vanadate materials such as CuV_2O_6 [27,29–31], $\text{Cu}_2\text{V}_2\text{O}_7$ [27–33], $\text{Cu}_3\text{V}_2\text{O}_8$ [28,32,34–36], $\text{Cu}_5\text{V}_2\text{O}_{10}$ [32], $\text{Cu}_{11}\text{V}_6\text{O}_{26}$ [28,32,37], and Cu_3VO_4 [38] have been utilized in PEC water splitting. It has been reported that a change in the stoichiometric ratio (Cu:V ratio) of copper vanadates alter their electrical and optical properties, that in turn affect its PEC water splitting performance [32]. Although there have been numerous studies on the PEC activity of CuV_2O_6 , $\text{Cu}_2\text{V}_2\text{O}_7$, and $\text{Cu}_3\text{V}_2\text{O}_8$, only a few studies have been carried out to investigate the PEC activity of Cu-rich $\text{Cu}_5\text{V}_2\text{O}_{10}$ and $\text{Cu}_{11}\text{V}_6\text{O}_{26}$.

In copper vanadates, the stoichiometric ratio of Cu:V can be controlled by using the co-sputtering synthesis method [28,32,35]. However, it is difficult to simultaneously control the morphology and Cu:V

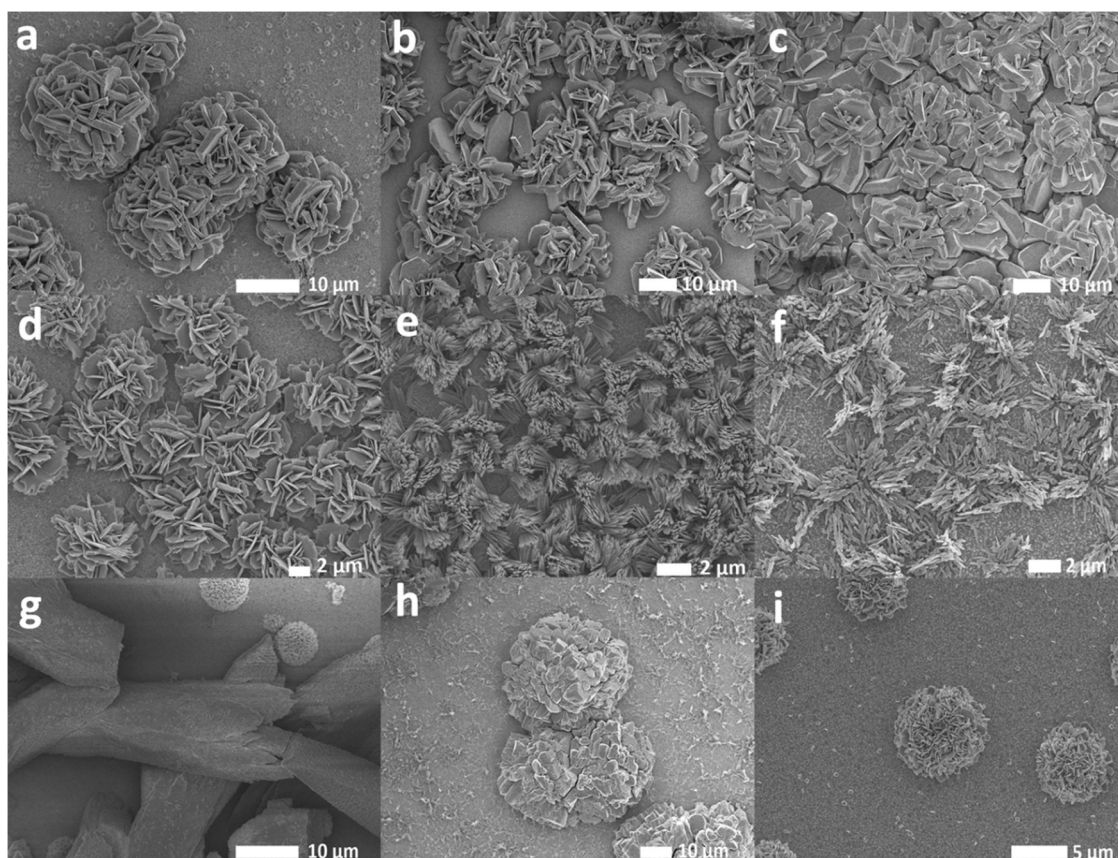


Fig. 2. Surface SEM image of CV1 synthesized in the presence of (a) 0.1, (b) 0.2, and (c) 0.25 M urea. Surface SEM image of CV2 synthesized in the presence of (d) 0.05, (e) 0.15, and (f) 0.2 M urea. Surface SEM image of CV3 synthesized in the presence of (g) 0.05, (h) 0.15, and (i) 0.2 M urea.

ratio using the co-sputtering method. Furthermore, other synthesis methods such as the drop casting [25,28], electrospray [31], dip coating [34], spin coating [36], and electrodeposition [37] methods involve multiple steps in thin film fabrication and do not allow much control over the Cu:V stoichiometric ratio and morphology at the same time. Among the copper vanadates, $\text{Cu}_2\text{V}_2\text{O}_7$ and Cu-rich $\text{Cu}_5\text{V}_2\text{O}_{10}$ and $\text{Cu}_{11}\text{V}_6\text{O}_{26}$ were the widely studied materials for PEC water oxidation. Literature survey revealed that $\text{Cu}_2\text{V}_2\text{O}_7$ could be obtained in various morphologies such as nanoparticles [30,31,33], nanograins [32] and sand-flower nanostructures [27] producing the highest photocurrent of 0.65 mA cm^{-2} [27,31]. Whereas, Cu-rich $\text{Cu}_5\text{V}_2\text{O}_{10}$ having nanograin morphology yields the highest photocurrent of 0.206 mA cm^{-2} [32]. Furthermore, the globular networks of Cu-rich $\text{Cu}_{11}\text{V}_6\text{O}_{26}$ were reported to produce the highest photocurrent of only 0.010 mA cm^{-2} [37]. Therefore, the choice of a suitable synthesis technique is highly crucial for obtaining the copper vanadates having desired morphology and stoichiometry.

Herein, we proposed a facile single-step hydrothermal method for the synthesis of $\text{Cu}_2\text{V}_2\text{O}_7$ and Cu-rich $\text{Cu}_5\text{V}_2\text{O}_{10}$ and $\text{Cu}_{11}\text{V}_6\text{O}_{26}$ thin films on fluorine-doped tin oxide (FTO) substrate for PEC water splitting. The morphology and stoichiometric Cu:V ratio of the copper vanadates developed in this study were found to be dependent on the amount of urea and the Cu:V ratio of the precursors used in the synthesis solution. By using an optimum amount of urea, $\text{Cu}_2\text{V}_2\text{O}_7$, $\text{Cu}_5\text{V}_2\text{O}_{10}$, and $\text{Cu}_{11}\text{V}_6\text{O}_{26}$ thin films with nanoplate, nanorods, and micropillar morphologies, respectively were obtained. The physical and chemical properties of these copper vanadate thin films were investigated in detail. Among the synthesized materials, $\text{Cu}_2\text{V}_2\text{O}_7$ exhibited the highest photocurrent of 0.41 mA cm^{-2} , whereas $\text{Cu}_{11}\text{V}_6\text{O}_{26}$ exhibited a low photocurrent of 0.076 mA cm^{-2} at 1.23 V vs. reversible hydrogen electrode (RHE) under 1-sun illumination. Importantly, the

nanorod structured $\text{Cu}_5\text{V}_2\text{O}_{10}$ showed a photocurrent of 0.27 mA cm^{-2} (at 1.23 V vs. RHE) under 1-sun illumination, which is the highest photocurrent reported till date for $\text{Cu}_5\text{V}_2\text{O}_{10}$. The band edge positions of the copper vanadate thin films were determined from their spectroscopic and electrochemical data.

2. Experimental

Copper vanadate nanostructures were directly grown on an FTO glass substrate using a single-step hydrothermal method. Copper sulfate (CuSO_4 , Sigma-Aldrich, $\geq 99.0\%$) and vanadyl acetylacetonate ($\text{C}_{10}\text{H}_{14}\text{O}_5\text{V}$, Sigma-Aldrich, $\geq 98.0\%$) were used as the copper and vanadium sources, respectively. Urea ($\text{CH}_4\text{N}_2\text{O}$, Sigma-Aldrich, $\geq 99.0\%$) was used as the structure directing agent for the successful hydrothermal deposition of the copper vanadates on the FTO substrate. Table S1 lists the amount of copper sulfate, vanadyl acetylacetonate, and urea used to prepare the hydrothermal synthesis solutions for the three types of copper vanadate thin films. For the thin film fabrication, the required hydrothermal synthesis solution (as in table S1) was transferred to a Teflon-lined autoclave (filling it to $< 70\%$) containing a pre-cleaned (cleaned and sonicated in distilled water, ethanol, and isopropanol sequentially) FTO substrate placed at an angle against the Teflon-liner with the conducting side facing down. The hydrothermal synthesis was carried out at 150°C for 5 h. After the synthesis, the autoclave was cooled, and the copper vanadate thin films were removed and washed with deionized water. All the synthesized thin films were then annealed in air at 500°C for 2 h (at a heating rate of 3°C min^{-1}) to obtain crystalline samples.

The crystalline structures of the copper vanadate thin films were examined using a MiniFlex (Japan) desktop X-ray diffraction (XRD) instrument using Cu K α radiation. The diffraction angle (2θ) was varied

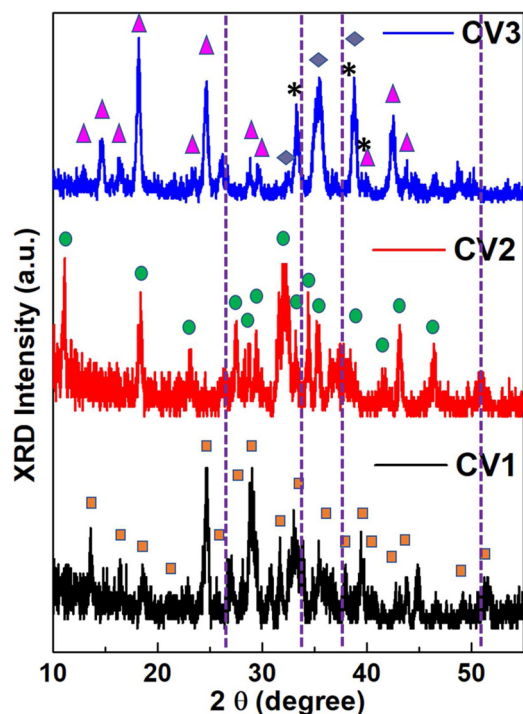


Fig. 3. XRD patterns of CV1 (black line), CV2 (red line) and CV3 (blue line). The purple lines represent the position of the SnO_2 peak arising from the substrate. In CV1, the orange squares represent the $\text{Cu}_2\text{V}_2\text{O}_7$ peaks. In CV2, the green dots represent the $\text{Cu}_5\text{V}_2\text{O}_{10}$ peaks. In CV3, the peaks corresponding to $\text{Cu}_{11}\text{V}_6\text{O}_{26}$, Cu_3VO_4 , and CuO are shown with pink triangles, asterisk, and gray rhombus symbols, respectively (For interpretation of the references to colour in this figure legend, the reader is referred to the web version of this article).

from 10 to 70°. The morphology (surface) and the thickness of the copper vanadate thin films were investigated using scanning electron microscopy (SEM; Hitachi S4800 (Japan)). The crystallinity and interplanar d-spacing of the films were examined in detail by carrying out transmission electron microscopy (TEM) measurements using a JEOL JEM-2100 F (USA) instrument. Elemental mapping and energy-dispersive X-ray spectroscopy (EDS) measurements were performed during the TEM measurements in the scanning transmission electron microscopy (STEM) mode using a nickel-carbon mesh-type grid. The ultraviolet-visible (UV–Vis) absorption spectra of the thin films were recorded in an integrated sphere in the scattering mode over the wavelength range of 200–800 nm using a Varian Cary 5000 spectrophotometer (Australia). X-ray photoelectron spectroscopy (XPS) analysis was carried out using a Thermo Fisher Scientific Co. (USA) theta probe angle-resolved X-ray photoelectron spectrometer with a monochromatic micro-focused Al K α (1486. 6 eV) source. The peak energy for the XPS measurements was self-calibrated to C 1s and O 1s reference peak states. An ABET Technologies Sun 2000 solar simulator (USA) calibrated to AM 1.5G irradiance conditions was used as the light source. Incident photon-to-current efficiency measurements were carried out using a Thermo Oriol 1000 W xenon arc lamp (Thermo Oriol 66902, USA) combined with a monochromator (Thermo Oriol Cornerstone 7400 1/8). PEC measurements were carried out on an Iviumstat (Netherlands) electrochemical analyzer.

The PEC measurements of the copper vanadate thin film photoanodes were carried out in a quartz cell containing a Pt counter electrode and an Ag/AgCl reference electrode in a 0.5 M Na_2SO_4 (pH 7.5) electrolyte. Linear sweep voltammetry was used to measure photocurrents with a scan rate of 50 mV s^{-1} between the potential range of 0.4–1.8 V vs. RHE. During the PEC measurements, all the electrodes were masked with an O ring, exposing an area of 0.125 cm^2 of the photoanode to the incident light source. The electrochemical

impedance spectroscopy (EIS) analysis of the thin films was carried out over the frequency range of 0.1–10⁵ Hz at 1.23 V vs. RHE using an alternating current voltage perturbation of 10 mV. Mott-Schottky (MS) measurements were carried out in a 0.5 M Na_2SO_4 (pH 7.5) electrolyte in the absence of irradiation at 1 kHz. The amount of O_2 produced during the PEC activity was measured using gas chromatography (YOUNG LIN - YL 6500 GC, South Korea) system, equipped with pulsed discharge ionization detector (PDD) containing capillary column. The gas collected in the sealed reaction cell was pumped into GC using helium carrier gas. The applied potential was converted with respect to the RHE values using the following Nernst equations:

$$E_{\text{RHE}} = E_{\text{Ag/AgCl}} + (0.0591 \times \text{pH}) + E^{\circ}_{\text{Ag/AgCl}} \quad (1)$$

$$E^{\circ}_{\text{Ag/AgCl}} (3.0\text{M NaCl}) = 0.209\text{V at } 25^{\circ}\text{C}$$

3. Results and discussion

Various copper vanadate thin films ($\text{Cu}_2\text{V}_2\text{O}_7$, $\text{Cu}_5\text{V}_2\text{O}_{10}$, and $\text{Cu}_{11}\text{V}_6\text{O}_{26}$) on FTO substrate were synthesized by controlling the ratio of Cu and V precursor concentration during the hydrothermal condensation. During the synthesis, the presence of urea was found to play a crucial role in the effective deposition of copper vanadate and directs its growth on the FTO substrate. No significant deposition was observed when the hydrothermal synthesis was carried out in the absence of urea. This indicates that the presence of urea and its concentration is crucial for the deposition of copper vanadate on FTO substrates. The amount of urea in the hydrothermal solution significantly affected the morphology of the copper vanadate thin films and their adhesion on the FTO surface. Table S1 lists the optimum amount of copper and vanadium precursors utilized to synthesize the $\text{Cu}_2\text{V}_2\text{O}_7$ (CV1), $\text{Cu}_5\text{V}_2\text{O}_{10}$ (CV2), and $\text{Cu}_{11}\text{V}_6\text{O}_{26}$ (CV3) thin films along with the optimum amount of urea (the amount of urea used to fabricate the photoelectrode that showed the highest photocurrent) required to produce stable (good adhesion) and uniform thin films. The optimum amount of urea for the synthesis of CV1, CV2, and CV3 was found to be 0.15, 0.1, and 0.1 M, respectively.

Scheme 1 shows the optimized synthesis condition and the resulting morphologies of copper vanadate thin films on FTO substrate. The morphology and the thickness of the synthesized copper vanadate films (at optimum urea amounts) were examined by SEM, as shown in Fig. 1. The surface SEM image shown in Fig. 1a reveals that CV1 (deposited on the FTO substrate) showed nanoplate morphology ensemble to form flower-like microstructures. The nanoplate thickness was found to be within the range 300–1000 nm. The average thickness of the CV1 film (Fig. 1b) was measured to be ~8 μm . As shown in Fig. 1c, CV2 showed nanorod morphology grouped to appear as grass-like structures. The thickness and length of the nanorods were found to be ~150 nm and 1 μm , respectively. However, the thickness of the film on the FTO substrate varied from ~7 to 10 μm (Fig. 1d). CV3 showed micropillars distributed randomly on the FTO surface (Fig. 1e). The length of the micropillars varied from ~10 to 50 μm with one end of the micropillars showing sharp edges. The overall thickness of the CV3 film was measured to be ~10 μm (Fig. 1f). Fig. S1 shows the high-resolution SEM images of the CV1, CV2, and CV3 thin films indicating that the copper vanadate nanostructures were uniformly deposited on the FTO substrate.

During the hydrothermal synthesis, both the ratio of Cu and V precursor concentration and the amount of urea was revealed to affect the morphology of copper vanadate thin films whereas the thin film formation and the adhesion of copper vanadate were found to be dependent only on the amount of urea. To investigate this, the concentration of Cu and V precursor solution and the urea were varied during the synthesis. Fig. 2 shows the surface SEM image of CV1, CV2 and CV3 thin films synthesized in the presence of different urea concentrations. That is, during the synthesis of CV1, the presence of 0.1 M

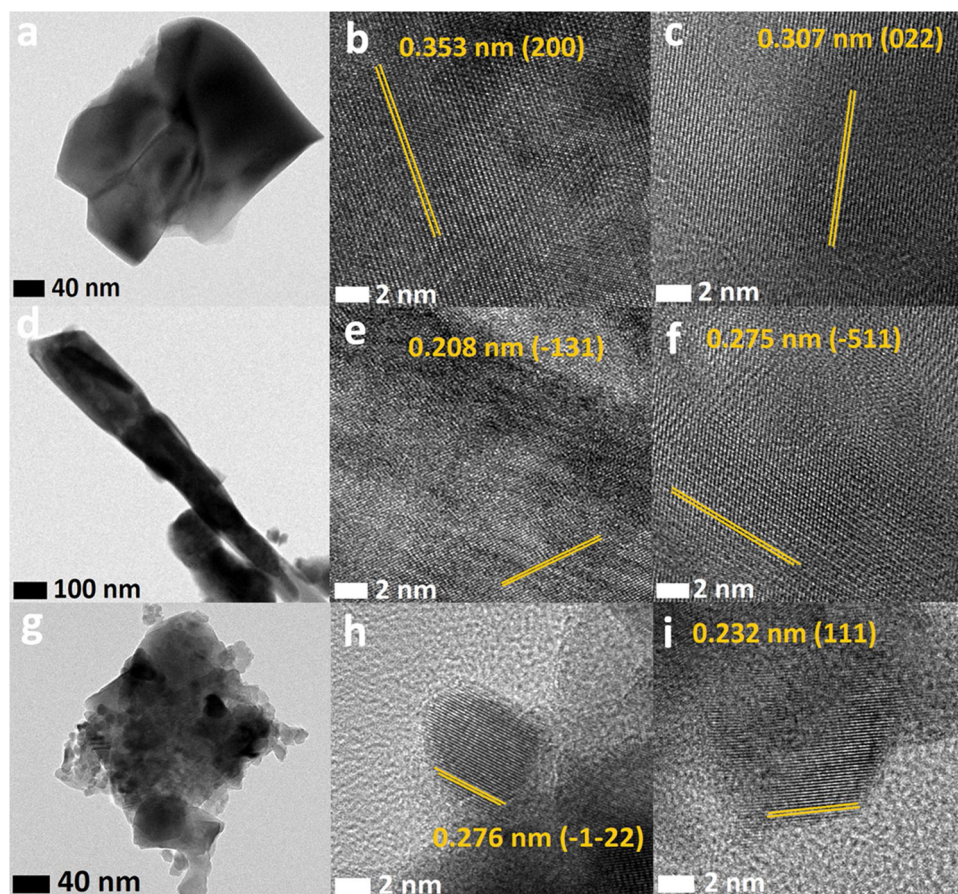


Fig. 4. (a) Low- and (b) (c) high-resolution TEM images of CV1. (d) Low- and (e) (f) high-resolution TEM images of CV2. (g) Low- and (h) (i) high-resolution TEM images of CV3.

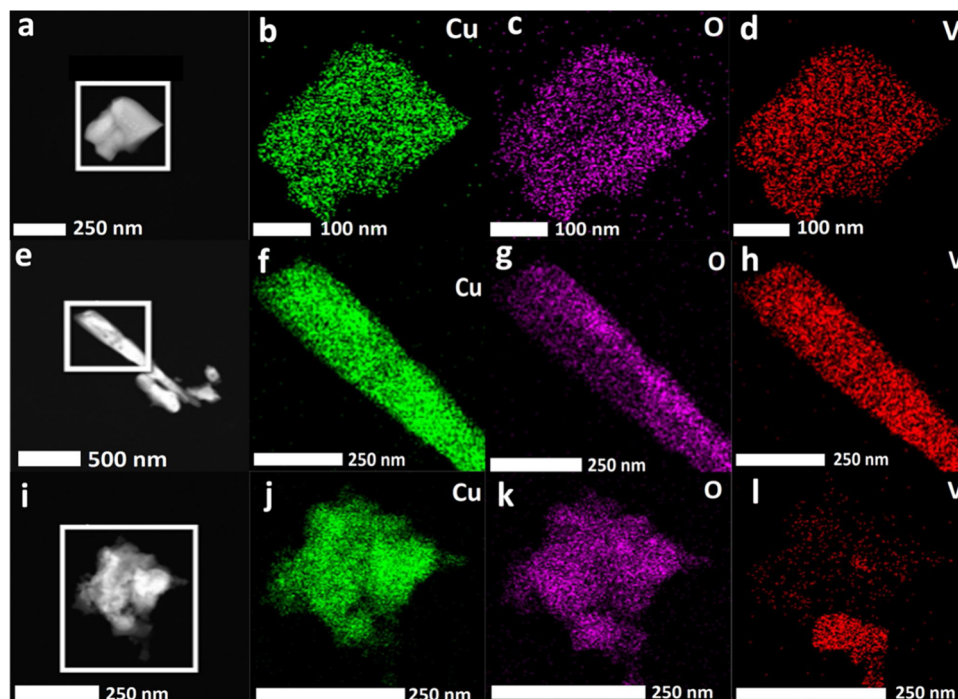


Fig. 5. STEM image with selected area for elemental mapping for (a) CV1, (e) CV2, and (i) CV3. Mapping of Cu (b), O (c), and V (d) in CV1. Mapping of Cu (f), O (g), and V (h) in CV2. Mapping of Cu (j), O (k), and V (l) in CV3.

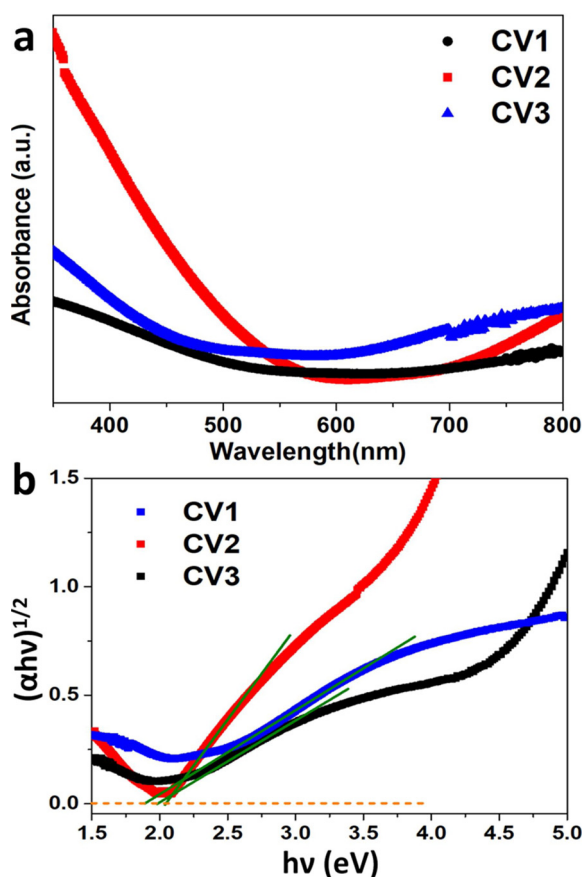


Fig. 6. (a) UV-vis absorption spectra and (b) Tauc plots of CV1 (black line), CV2 (red line), and CV3 (blue line) (For interpretation of the references to colour in this figure legend, the reader is referred to the web version of this article).

urea in the solution yielded thick nanoplates (as compared to those obtained when 0.15 M urea was used) with a micro-flower morphology (Fig. 2a). A higher urea concentration of 0.2 M yielded CV1 nanoplates distributed randomly on the FTO substrate, as shown in Fig. 2b. With a further increase in the urea concentration to 0.25 M, the distribution of the nanoplates became more random (Fig. 2c). Here, it can be revealed that due to the constant concentration ratio between Cu and V, the morphology of CV1 remained to be nanoplate structure, and the variation in urea concentration caused the alteration in nanoplate thickness, its arrangement, and distribution. This indicates that the formation of nanoplate morphology in case CV1 was due to the type and concentration of Cu and V precursor. In the case of CV2, low concentrations of urea (0.05 M) produced nanoflakes with a flower-like morphology (Fig. 2d). As shown Fig. 2e, at urea contents higher than the optimum concentration, nanorods with a comparatively less dense arrangement were obtained. A further increase in the urea concentration reduced the deposition of CV2 nanorods on the FTO substrate (Fig. 2f). Importantly, it was revealed that the ratio of Cu and V maintained during the CV2 synthesis yields nanorod morphology despite utilizing the similar amount of urea as in case of CV1 synthesis. CV3 showed similar morphologies at 0.05 M and the optimum urea concentrations (Fig. 2g). However, at the urea concentrations higher than the optimum level, the morphology of CV3 changed drastically from micropillars to nanoparticles (Fig. 2h) and thick nanoflakes (Fig. 2i) at isolated places on the FTO substrate. The above observations indicated that the ratio of Cu and V concentration along with the amount of urea controls the final morphology of the product, whereas the adhesion and the thin film formation on FTO were dependent only on the amount of urea.

Fig. 3 shows the XRD patterns of the CV1, CV2, and CV3 thin films on the FTO substrate. The peaks corresponding to SnO_2 arising from the FTO substrate could not be observed because of the thick layer of the copper vanadate thin films. CV1 (Fig. 3) showed a single $\text{Cu}_2\text{V}_2\text{O}_7$ monoclinic phase (JCPDS 26-0569) [32,39]. The diffraction peaks of CV2 could be indexed to the $\text{Cu}_5\text{V}_2\text{O}_{10}$ monoclinic phase (JCPDS card, PDF no. 33-0504) [32,40]. The close observation of the diffraction peaks of CV3 revealed the co-existence of multiple copper vanadate phases. The diffraction peaks of CV3 were indexed to copper-rich $\text{Cu}_{11}\text{V}_6\text{O}_{26}$ [32,37] and Cu_3VO_4 [38]. In addition, the diffraction peaks corresponding to p-type CuO [41] were also observed, indicating that multiple phases were formed at large Cu precursor amounts. Fig. 4 shows the TEM images of the synthesized copper vanadates. CV1, CV2, and CV3 showed nanoplate, nanorod, and nanoparticle/flake morphologies, respectively (low-resolution TEM images shown in Fig. 4a, d, and g, respectively). CV1 (high-resolution TEM (HR-TEM) images shown in Fig. 4b and c) showed inter-planar d-spacing values of 0.353 and 0.307 nm attributing to the (200) and (022) planes of monoclinic $\text{Cu}_2\text{V}_2\text{O}_7$. The interplanar d-spacing values of 0.208 and 0.275 nm shown in Fig. 4e and f, respectively can be attributed to the (-131) and (-511) planes of the $\text{Cu}_5\text{V}_2\text{O}_{10}$ phase. The TEM images of CV3 revealed that it showed d-spacing values corresponding to $\text{Cu}_{11}\text{V}_6\text{O}_{26}$ and CuO. This is consistent with the XRD results. From Fig. 4h and i, it can be observed that CV3 showed interplanar d-spacing values of 0.276 and 0.232 corresponding to the (-1-22) plane of $\text{Cu}_{11}\text{V}_6\text{O}_{26}$ and (111) plane of CuO, respectively. However, despite carrying out TEM observations at various positions, the d-spacing value corresponding to the Cu_3VO_4 phase could not be determined. Furthermore, Fig. S2 shows the HR-TEM images of $\text{Cu}_2\text{V}_2\text{O}_7$ and $\text{Cu}_5\text{V}_2\text{O}_{10}$ in CV3 and the corresponding d-spacing values. The images also showed that $\text{Cu}_{11}\text{V}_6\text{O}_{26}$ phase was predominant in CV3.

High-angle annular dark-field STEM imaging along with elemental mapping was employed to quantify and analyze the distribution of Cu, V, and O in CV1, CV2, and CV3. Fig. 5 shows the STEM images and elemental mapping results of CV1, CV2, and CV3. From Fig. 5b–d it can be observed that in CV1, both Cu and V were distributed uniformly without any significant agglomeration. Fig. S3 shows that CV1 consisted of Cu, V, and O without any impurity confirming the existence of pure $\text{Cu}_2\text{V}_2\text{O}_7$. Similarly, elemental mapping shown in Fig. 5f–h reveal that Cu, V, and O were distributed uniformly in CV2. Fig. S4 confirms the presence of pure $\text{Cu}_5\text{V}_2\text{O}_{10}$ in CV2. However, in the case of CV3, Cu and V were unevenly distributed, and V was not detected in a few areas (Fig. 5j–l and S5). This can be attributed to the presence of multiple phases in CV3 ($\text{Cu}_{11}\text{V}_6\text{O}_{26}$, Cu_3VO_4 , and CuO), as confirmed by the XRD results. The undetected V in Fig. 5l can be attributed to the presence of CuO. The stoichiometric ratio of Cu:V in copper vanadates affects their optical properties (bandgap). Generally, an increase of the copper content in copper vanadate materials causes a red shift in their absorption [29]. As shown in Fig. 6a, all the copper vanadate thin films showed absorbance until ~600 nm. This is consistent with the results reported previously. Copper vanadates also show absorbance below the bandgap energy, suggesting the presence of interband states [37]. The indirect bandgaps of the copper vanadate thin films were determined by analyzing their Tauc plots as shown in Fig. 6b. The Tauc plots of all the copper vanadate phases showed a clear linear region with extrapolated bandgap energies in the range of 1.8–2.0 eV [28]. The bandgaps of CV1, CV2, and CV3 were found to be 1.98, 2.03, and 1.85 eV, respectively, which are consistent with the previously reported values [28,30,32].

XPS measurements were carried out to gain a deeper insight into the chemical composition of the synthesized copper vanadates. All the copper vanadate materials showed Cu 2p characteristic peaks centered at ~935 and ~955 eV corresponding to Cu 2p_{3/2} and Cu 2p_{1/2}, respectively (Fig. 7a). In addition to the main peaks, a series of satellite peaks appeared at ~942.5 and ~962.5 eV corresponding to Cu 2p_{3/2} and Cu 2p_{1/2}, respectively, indicating the existence of an unfilled Cu 3d shell [42]. Careful observation of Fig. 7a reveals that the shape of the Cu 2p peak

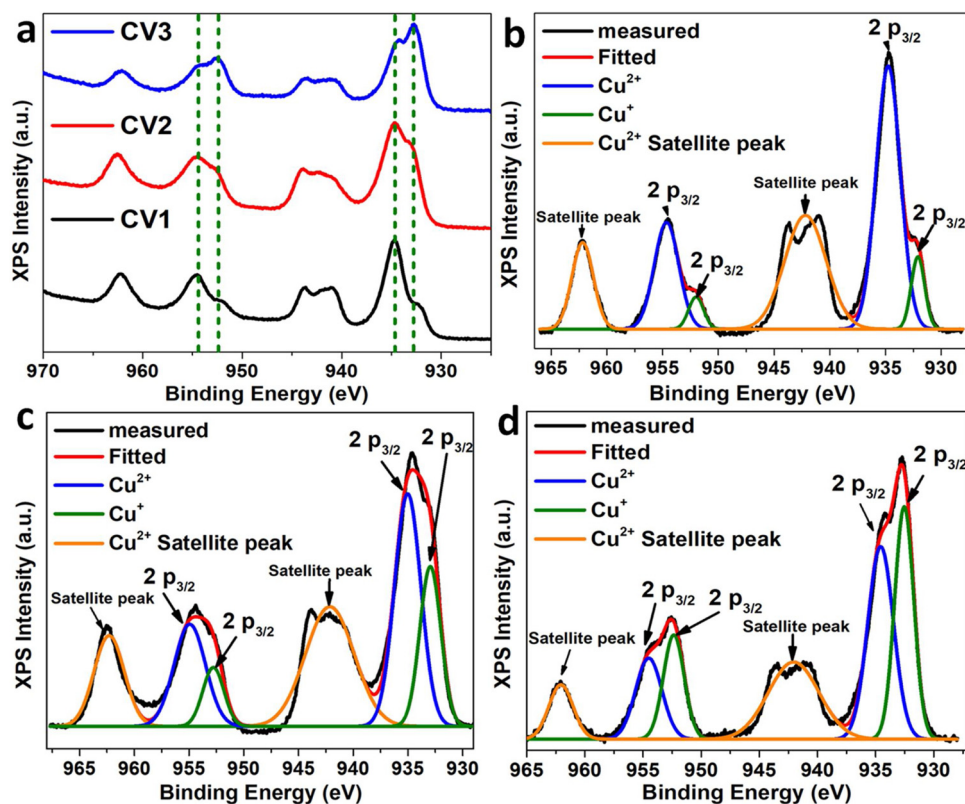


Fig. 7. Overlapped (a) Cu 2p_{3/2} XPS spectra of CV1 (black line), CV2 (red line), and CV3 (blue line). Deconvoluted XPS spectra of the Cu 2p core level of (b) CV1, (c) CV2, and (d) CV3. (For interpretation of the references to colour in this figure legend, the reader is referred to the web version of this article).

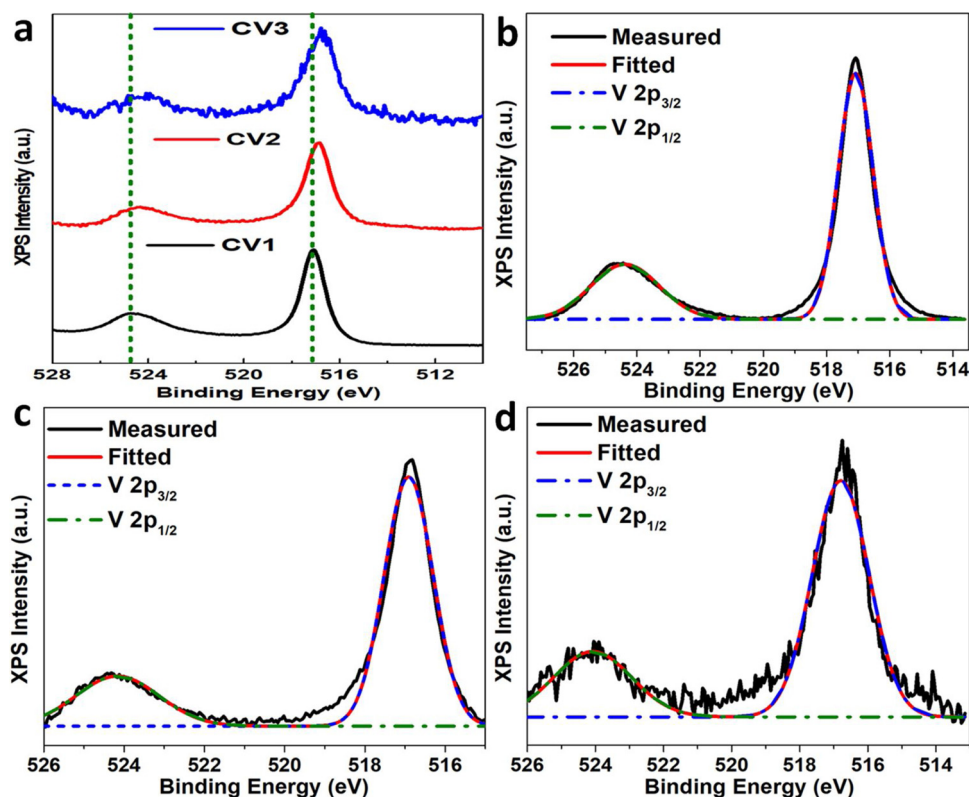


Fig. 8. Overlapped (a) V 2p XPS spectra of CV1 (black line), CV2 (red line), and CV3 (blue line). Deconvoluted XPS spectra of the V 2p core level of (b) CV1, (c) CV2, and (d) CV3. (For interpretation of the references to colour in this figure legend, the reader is referred to the web version of this article).

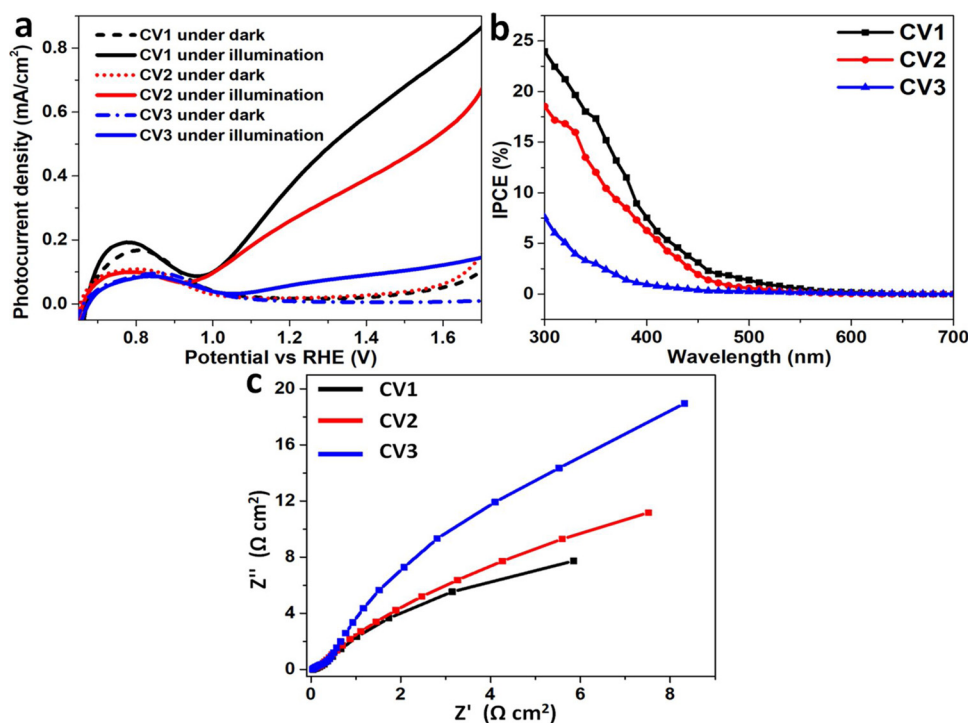


Fig. 9. (a) LSV curves of CV1 (black line), CV2 (red line), and CV3 (blue line) obtained in 0.1 M Na₂SO₄ with (solid lines) and without (dotted lines) 1.5 G illumination at a scan rate of 50 mVs⁻¹. (b) IPCE of CV1 (black line), CV2 (red line), and CV3 (blue line) measured at a bias potential of 1.23 V vs. RHE in 0.1 M Na₂SO₄. (c) Nyquist curves under AM 1.5 G illumination of CV1 (black line), CV2 (red line), and CV3 (Blue line) obtained at 1.23 V vs. RHE in 0.1 M Na₂SO₄.

changed significantly with an increase in the Cu content from CV1 to CV2 to CV3 without shifting the peak positions. To elucidate this mechanism the Cu 2p peaks were deconvoluted yielding two additional peaks for Cu 2p_{3/2} and Cu 2p_{1/2} [43]. The deconvolution of Cu 2p XPS produces two peaks which were assigned to either Cu⁺ or Cu²⁺ based on the peak positions. Generally, the XPS peaks of Cu²⁺ state appear at high binding energy positions compared to Cu⁺ peaks [44]. Importantly, the areas of the Cu⁺ and Cu²⁺ peaks changed significantly with an increase in the Cu content of the copper vanadates (from CV1 to CV2 to CV3). As shown in Fig. 7b, in the case of CV1, the intensity of the Cu²⁺ peak was noticed to be significantly higher than that of the Cu⁺ peak. Whereas, in the case of CV2 (with higher Cu content), the area of the Cu⁺ peak was higher than that of the Cu²⁺ peak (Fig. 7c). In the case of CV3, the area of the Cu⁺ peak was higher than that of the Cu²⁺ peak (Fig. 7d). These observations indicate that an increase in the Cu content of the copper vanadates affected their valency. Fig. 8a shows the overlapped core level XPS survey spectra of V for CV1, CV2, and CV3. The XPS spectra of all the copper vanadate materials showed doublet with respect to 1/2 and 3/2 spin-orbit components of V 2p at ~524.5 and ~517.5 eV, respectively [45]. However, the V 2p peak position shifted significantly towards lower binding energies with an increase in the Cu content from CV1 to CV2 to CV3 which is in agreement with the results reported by Jiang et al. [32]. The deconvolution of V 2p peaks produced only one peak corresponding to the V⁵⁺ state (Fig. 8b-d). This indicates that in the copper vanadates, V was present in the (V) state, and the V⁴⁺ state was absent in all the synthesized copper vanadate materials. The significant noise observed in the V 2p spectra of CV3 (Fig. 8d) can be attributed either to the lower amounts of V in CV3 or the presence of CuO.

The PEC properties of the synthesized copper vanadates were evaluated by J–V measurements under AM1.5 G illumination in a 0.5 M Na₂SO₄ electrolyte. The J–V plots (for optimized thin films) of CV1, CV2, and CV3 are shown in Fig. 9a. A negligible current was observed in the absence of illumination for all the copper vanadate thin films. On the other hand, under illumination, CV1, CV2, and CV3 showed the maximum photocurrents of ~0.41, ~0.27, and ~0.076 mAcm⁻² at 1.23 V vs. RHE. Fig. S6 shows the photocurrent (at 1.23 V vs. RHE) produced by CV1, CV2, and CV3 as a function of the synthesis time interval. The

optimum synthesis times of the copper vanadates were determined from these curves. Table S2 compares the photocurrent values of the copper vanadates prepared in this study with those reported previously. In particular, the photocurrent produced by nanoplate Cu₂V₂O₇ thin film in this study was found to be one of the highest compared to the literature values [27,30–33]. The high photocurrent exhibited by Cu₂V₂O₇ thin films could be due to the nanoplate morphology which possesses fewer grain boundaries that decreases the hole diffusion length causing better separation of photogenerated charges. Whereas, the Cu-rich Cu₅V₂O₁₀ thin films having the unique nanorod morphology exhibited the highest photocurrent compared to nanoparticle morphology Cu₅V₂O₁₀ reported by Jiang et al. [32]. The record photocurrent noticed in case of Cu₅V₂O₁₀ thin films was ascribed to the unique one-dimensional (1-D) morphology that offers direct electrical pathways for the photogenerated charges along the nanorods structure [18]. Hence, compared to nanograin morphology, the reported 1-D nanostructure contains a high interfacial contact area that could increase the density of redox-active sites and enhance light harvesting ability. Furthermore, the micropillar morphology of Cu-rich Cu₁₁V₆O₂₆ produced the highest photocurrent of 0.076 mA cm⁻² which was found to be significantly higher than the globular network morphology reported earlier by Lumley et al. [37] and slightly higher than the nanograin morphology synthesized by Jiang et al. [32]. This indicates that the novel synthesis method proposed in this work produces efficient Cu₅V₂O₁₀ and Cu₁₁V₆O₂₆ photoanodes having the nanorod and micropillar morphology, respectively.

The incident photon-to-current efficiencies (IPCEs) of the synthesized copper vanadate thin films were measured at an applied bias potential of 1.23 V vs. RHE in 0.5 M Na₂SO₄, as shown in Fig. 9b. The IPCE of the copper vanadates was calculated as:

$$\text{IPCE (\%)} = [(1240 \times I_{\text{ph}}) / (\lambda \times J_{\text{light}})] \times 100 \quad (2)$$

Where I_{ph} is the photocurrent density, λ is the wavelength of the incident light, and J_{light} is the measured photocurrent at a specific wavelength. The IPCE values of CV1, CV2, and CV3 at 300 nm were found to be 24%, 18%, and 7.5%, respectively, which are the highest reported till date for these materials. Furthermore, the employed light source was validated for true AM 1.5 G solar simulation by calculating

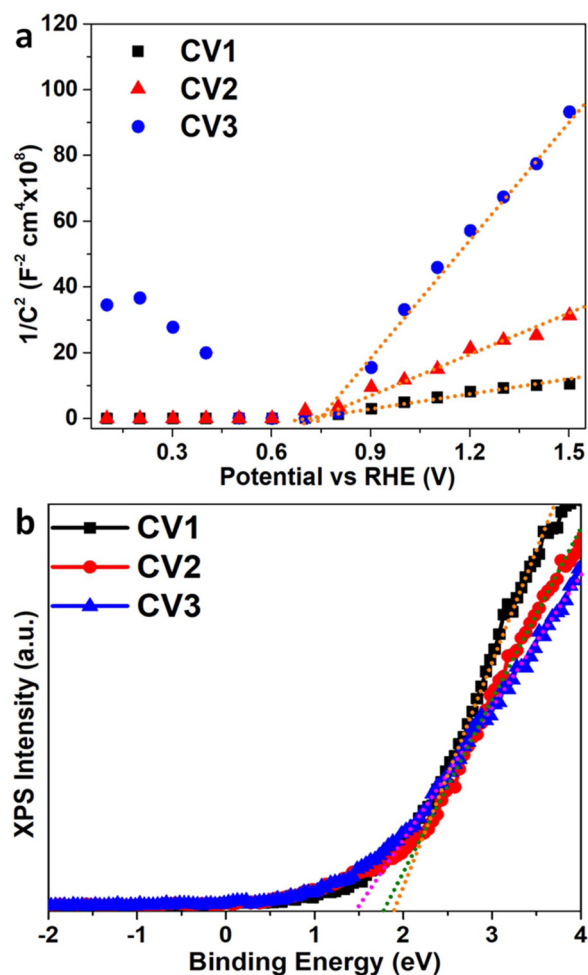


Fig. 10. (a) MS plots of CV1 (black line), CV2 (red line), and CV3 (blue line) obtained in 0.1 M Na₂SO₄ at 1 kHz. (b) XPS valence band edge graph of CV1 (black line), CV2, (red line) and CV3 (blue line). (For interpretation of the references to colour in this figure legend, the reader is referred to the web version of this article).

the photocurrent values by integrating the IPCE values with the standard solar AM 1.5 spectrum. As shown in Fig. S7 the photocurrent values of CV1, CV2, and CV3 obtained by integrating their IPCE values over the wavelength range of 300–700 nm were 0.37, 0.25, and 0.063 mA cm⁻², respectively. These values are consistent with those obtained under 1-sun illumination. EIS analysis was carried out to investigate the charge transfer properties of the CV1, CV2, and CV3 thin

films at the electrode/electrolyte interface. From the Nyquist plots (shown in Fig. 9c) of the thin films, it can be observed that CV1 exhibited a smaller semicircle region than CV2, whereas CV3 showed the largest semicircle region. This indicates that among the synthesized copper vanadates, CV1 showed the lowest charge transfer resistance at the electrode/electrolyte interface. The stability of the synthesized copper vanadate thin films was investigated using chronoamperometry technique in 0.5 M Na₂SO₄ electrolyte at an applied bias potential of 1.23 V vs. RHE (Fig. S8a). All the copper vanadate thin films (CV1, CV2, and CV3) exhibited good stability under the PEC water splitting condition over the tested time without any significant electrode/photo-current degradation. That is, after the 3 h of PEC water splitting conditions, the copper vanadate thin films were found to retain at least 85% of their initial photocurrent values. This indicates that the synthesized copper vanadate thin films are stable under the continuous irradiation and water oxidation reactions. Furthermore, the photocurrent generated was revealed to be due to the water oxidation which was determined using GC. Fig. S8b shows the quantified amount of O₂ generated at the copper vanadate photoanode during the PEC conditions. Among the thin films, CV1 photoanode generated higher amounts of O₂ compared to CV2, whereas CV3 produced extremely low amounts of O₂ under the illumination. The faradaic efficiencies of O₂ gas evolutions of CV1, CV2, and CV3 photoanodes were calculated using the following equation:

$$\text{Faradaic efficiency} = (4F \times n_{\text{O}_2})/Q \quad (3)$$

where n_{O_2} is the total amount of oxygen produced (mol), Q is the total amount of charge (C) and F is the Faraday constant. Here it is considered that the four electrons are needed to produce one O₂ molecule. Based on this, the Faradaic efficiencies of CV1, CV2, and CV3 were calculated to be 88%, 86% and 79%, respectively.

The flat-band potential (V_{FB}) and carrier density (N_D) values of the synthesized copper vanadates were determined via MS analysis using the following equation:

$$1/C^2 = [2/(N_D e \epsilon_0 \epsilon)] [(V_S - V_{\text{FB}}) - (k_B T/e)] \quad (4)$$

where C is the space charge capacitance, V_S is the applied potential, N_D is the electron carrier density, ϵ_0 is the permittivity of the vacuum, ϵ is the relative permittivity of the semiconductor, e is the elementary charge, T is temperature (298 K), and k_B is the Boltzmann constant. Based on the reported article, the value of the relative dielectric permittivity (ϵ) was assumed to be 44 [36]. The $1/C^2$ vs. applied potential plots of both CV1 and CV2 showed positive slopes (Fig. 10a), confirming that these thin films were n-type semiconductors with electrons as the charge carriers. However, the MS plot of CV3 showed both positive and negative slopes because of the presence of Cu₁₁V₆O₂ and CuO, respectively. The flat-band potential (V_{FB}) values of CV1, CV2, and CV3, as obtained from the intercepts of the MS plots, were found to

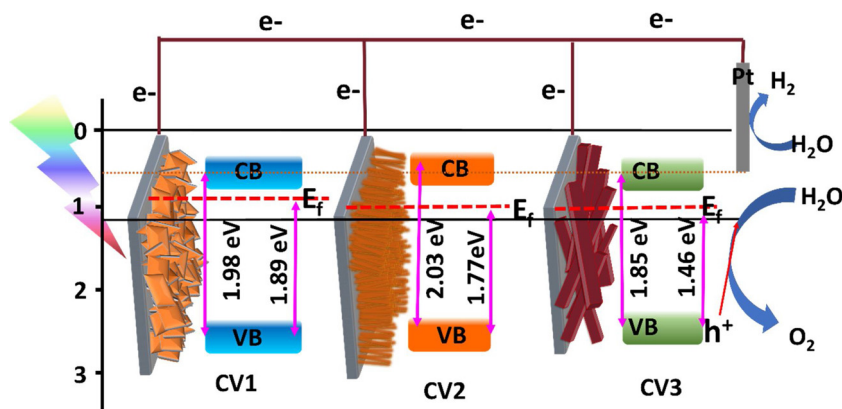


Fig. 11. Band edge position diagrams of CV1, CV2, and CV3 obtained using the electrochemical and spectroscopic data.

be ~0.704 V, 0.665 V, and 0.69, respectively. This indicates that an increase in the Cu content caused a negative shift in the flat band potentials of the copper vanadates. Furthermore, the carrier density N_D values of the copper vanadate thin films were calculated using the following equation:

$$N_D = -[2/(e\epsilon_0\epsilon)] [d(1/C^2)/d(U_s)]^{-1} \quad (5)$$

The values of N_D for CV1, CV2, and CV3 were calculated to be 2.37×10^{19} , 8.97×10^{18} , and $2.07 \times 10^{18} \text{ cm}^{-3}$, respectively. Fig. 10b shows the XPS valence band edge graphs of the synthesized copper vanadates. From these plots, the energy difference between the Fermi level and the valence band edge for CV1, CV2, and CV3 was measured to be 1.89, 1.77, and 1.46 eV, respectively. This indicates that an increase in the Cu content pushed the Fermi level of the copper vanadates downwards towards the valence band from CV1 to CV2 to CV3. These observations reveal that CV1 was more n-type than CV2, which was more n-type than CV3. The poor n-type characteristics of CV3 can be attributed to the presence of p-type CuO.

The flat band potential of n-type semiconductors is often considered to be more positive than their conduction band edge position [46]. In general, the conduction band edge position is believed to lie ~0.1 eV above the flat band potential [30]. Hence, based on this assumption the conduction band edge positions (vs. RHE) of CV1, CV2, and CV3 were calculated to be 0.604, 0.565, and 0.590 eV, respectively. The valence band edge and Fermi level positions of the thin films could be determined using their approximate band edge positions. Based on these calculations, the band edge position of CV1, CV2, and CV3 with respect RHE potential were determined, as shown in Fig. 11. It was found that an increase in the Cu content (from $\text{Cu}_2\text{V}_2\text{O}_7$ to $\text{Cu}_{11}\text{V}_6\text{O}_{26}$ and to $\text{Cu}_5\text{V}_2\text{O}_{10}$) caused a cathodic shift in the flat band potentials of the copper vanadates. This shifted both conduction and valence band edge positions upwards with respect to RHE. In contrast, the Fermi level position of the copper vanadates shifted down towards the valence band edge position with an increase in the Cu content. Furthermore, with an increase in the Cu content, the carrier density values of the vanadates decreased and the $\text{Cu}^{2+}:\text{Cu}^+$ ratio decreased. This affected the PEC activity of the copper vanadates. Thus, the photocurrent of $\text{Cu}_2\text{V}_2\text{O}_7$ was higher than those of $\text{Cu}_5\text{V}_2\text{O}_{10}$ or $\text{Cu}_{11}\text{V}_6\text{O}_{26}$. The copper vanadate with higher carrier density values and Cu^{2+} content along with lower Cu:V ratio showed better PEC results. Whereas, the copper vanadates with higher Cu:V ratios showed lower carrier densities and Cu^{2+} contents, and hence exhibited poor PEC activities. Overall, the copper vanadates synthesized in the present work exhibited unique and favorable morphology with tuned compositions and thus demonstrated improved PEC properties. Thus, the results of this study can be used to design copper vanadates for high-efficiency PEC water splitting applications.

4. Conclusion

A facile single-step hydrothermal method was developed for the synthesis of $\text{Cu}_2\text{V}_2\text{O}_7$ nanoplates, $\text{Cu}_5\text{V}_2\text{O}_{10}$ nanorods, and $\text{Cu}_{11}\text{V}_6\text{O}_{26}$ micropillars on an FTO substrate without using a seed layer. The presence of urea during the hydrothermal synthesis played a crucial role in thin film formation and significantly affected the morphology of the copper vanadates. The results showed that $\text{Cu}_2\text{V}_2\text{O}_7$ and $\text{Cu}_5\text{V}_2\text{O}_{10}$ consisted of a single phase, whereas $\text{Cu}_{11}\text{V}_6\text{O}_{26}$ consisted of multiple phases including Cu_3VO_4 and CuO. EDS mapping showed that the distribution of Cu and V in $\text{Cu}_2\text{V}_2\text{O}_7$ and $\text{Cu}_5\text{V}_2\text{O}_{10}$ was uniform, while that in $\text{Cu}_{11}\text{V}_6\text{O}_{26}$ was non-uniform, confirming the presence of multiple phases in it. The optical measurements showed that an increase in the Cu content of the copper vanadates from $\text{Cu}_2\text{V}_2\text{O}_7$ to $\text{Cu}_5\text{V}_2\text{O}_{10}$ to $\text{Cu}_{11}\text{V}_6\text{O}_{26}$ decreased their bandgaps. The deconvoluted Cu 2p XPS spectra showed the Cu^{2+} and Cu^+ peak areas of the copper vanadates changed significantly with an increase in their Cu contents. The

optimized $\text{Cu}_2\text{V}_2\text{O}_7$, $\text{Cu}_5\text{V}_2\text{O}_{10}$, and $\text{Cu}_{11}\text{V}_6\text{O}_{26}$ electrodes synthesized in this study exhibited the photocurrent densities of ~0.41, ~0.27, and ~0.076 mA cm^{-2} at 1.23 V vs. RHE under 1-sun illumination, respectively. These values are the highest reported till date for these materials. The highest IPCE values of the $\text{Cu}_2\text{V}_2\text{O}_7$, $\text{Cu}_5\text{V}_2\text{O}_{10}$, and $\text{Cu}_{11}\text{V}_6\text{O}_{26}$ electrodes at 300 nm were found to be 24%, 18%, and 7.5%, respectively. The band edge positions of $\text{Cu}_2\text{V}_2\text{O}_7$, $\text{Cu}_5\text{V}_2\text{O}_{10}$, and $\text{Cu}_{11}\text{V}_6\text{O}_{26}$ were determined using their spectroscopic and electrochemical data. These results showed that by controlling the Cu:V ratio and nanostructuring, copper vanadates with excellent PEC activity can be prepared for water splitting applications.

Acknowledgments

This work was supported by the basic Research & Development program [NRF-2017R1D1A1B03035201 and NRF-2019R1A2C2003804] of the Ministry of Science and ICT, Republic of Korea. This work was also supported by Ajou University.

Appendix A. Supplementary data

Supplementary material related to this article can be found, in the online version, at doi:<https://doi.org/10.1016/j.apcatb.2019.02.069>.

References

- [1] S.S. Kalanur, L.T. Duy, H. Seo, Recent progress in photoelectrochemical water splitting activity of WO_3 photoanodes, *Top. Catal.* 61 (2018) 1043–1076, <https://doi.org/10.1007/s11244-018-0950-1>.
- [2] B.S. Kalanoor, H. Seo, S.S. Kalanur, Recent developments in photoelectrochemical water-splitting using $\text{WO}_3/\text{BiVO}_4$ heterojunction photoanode: a review, *Mater. Sci. Energy Technol.* 1 (2018) 49–62, <https://doi.org/10.1016/j.mset.2018.03.004>.
- [3] M. Ahmed, G. Xinxi, A review of metal oxynitrides for photocatalysis, *Inorg. Chem. Front.* 3 (2016) 578–590, <https://doi.org/10.1039/C5QI00202H>.
- [4] F.E. Osterloh, Inorganic nanostructures for photoelectrochemical and photocatalytic water splitting, *Chem. Soc. Rev.* 42 (2013) 2294–2320, <https://doi.org/10.1039/C2CS35266D>.
- [5] Y. Liu, X. Xu, J. Zhang, H. Zhang, W. Tian, X. Li, M.O. Tade, H. Sun, S. Wang, Flower-like MoS_2 on graphitic carbon nitride for enhanced photocatalytic and electrochemical hydrogen evolutions, *Appl. Catal. B Environ.* 239 (2018) 334–344, <https://doi.org/10.1016/j.apcatb.2018.08.028>.
- [6] S.Y. Tee, K.Y. Win, W.S. Teo, L.-D. Koh, S. Liu, C.P. Teng, M.-Y. Han, Recent progress in energy-driven water splitting, *Adv. Sci.* 4 (2017) 1600337, <https://doi.org/10.1002/adv.201600337>.
- [7] M. Datt Bhatt, J. Sung Lee, Recent theoretical progress in the development of photoanode materials for solar water splitting photoelectrochemical cells, *J. Mater. Chem. A Mater. Energy Sustain.* 3 (2015) 10632–10659, <https://doi.org/10.1039/C5TA00257E>.
- [8] M.G. Walter, E.L. Warren, J.R. McKone, S.W. Boettcher, Q. Mi, E.A. Santori, N.S. Lewis, Solar water splitting cells, *Chem. Rev.* 110 (2010) 6446–6473, <https://doi.org/10.1021/cr1002326>.
- [9] T.J. Jacobsson, V. Fjällström, M. Edoff, T. Edvinsson, Sustainable solar hydrogen production: from photoelectrochemical cells to PV-electrolyzers and back again, *Energy Environ. Sci.* 7 (2014) 2056–2070, <https://doi.org/10.1039/C4EE00754A>.
- [10] S.S. Kalanur, H. Seo, Intercalation of barium into monoclinic tungsten oxide nanoplates for enhanced photoelectrochemical water splitting, *Chem. Eng. J.* 355 (2019) 784–796, <https://doi.org/10.1016/j.cej.2018.08.210>.
- [11] A. Fujishima, K. Honda, Electrochemical photolysis of water at a semiconductor electrode, *Nature* 238 (1972) 238037a0, <https://doi.org/10.1038/238037a0>.
- [12] H. Zhang, W. Tian, Y. Li, H. Sun, M.O. Tade, S. Wang, Heterostructured $\text{WO}_3/\text{CoWO}_4$ bilayer nanosheets for enhanced visible-light photo, electro and photoelectro-chemical oxidation of water, *J. Mater. Chem. A Mater. Energy Sustain.* 6 (2018) 6265–6272, <https://doi.org/10.1039/C8TA00555A>.
- [13] Y. Yang, S. Niu, D. Han, T. Liu, G. Wang, Y. Li, Progress in developing metal oxide nanomaterials for photoelectrochemical water splitting, *Adv. Energy Mater.* 7 (2017) 1700555, <https://doi.org/10.1002/aenm.201700555>.
- [14] C. Jiang, S.J.A. Moniz, A. Wang, T. Zhang, J. Tang, Photoelectrochemical devices for solar water splitting – materials and challenges, *Chem. Soc. Rev.* 46 (2017) 4645–4660, <https://doi.org/10.1039/C6CS00306K>.
- [15] T. Yao, X. An, H. Han, J.Q. Chen, C. Li, Photoelectrocatalytic materials for solar water splitting, *Adv. Energy Mater.* 8 (2018) 1800210, <https://doi.org/10.1002/aenm.201800210>.
- [16] H. Xu, R.Q. Zhang, A.M.C. Ng, A.B. Djurišić, H.T. Chan, W.K. Chan, S.Y. Tong, Splitting water on metal oxide surfaces, *J. Phys. Chem. C* 115 (2011) 19710–19715, <https://doi.org/10.1021/jp2032884>.
- [17] H. Cui, W. Zhao, C. Yang, H. Yin, T. Lin, Y. Shan, Y. Xie, H. Gu, F. Huang, Black TiO₂ nanotube arrays for high-efficiency photoelectrochemical water-splitting, *J. Mater. Chem. A Mater. Energy Sustain.* 2 (2014) 8612–8616, <https://doi.org/10.1039/C3TA00000A>.

- 1039/C4TA00176A.
- [18] S.S. Kalanur, Y.J. Hwang, S.Y. Chae, O.S. Joo, Facile growth of aligned WO_3 nanorods on FTO substrate for enhanced photoanodic water oxidation activity, *J. Mater. Chem. A Mater. Energy Sustain.* 1 (2013) 3479–3488, <https://doi.org/10.1039/C3TA01175E>.
 - [19] X. Ren, A. Sangle, S. Zhang, S. Yuan, Y. Zhao, L. Shi, R.L.Z. Hoye, S. Cho, D. Li, J.L. MacManus-Driscoll, Photoelectrochemical water splitting strongly enhanced in fast-grown ZnO nanotree and nanocluster structures, *J. Mater. Chem. A Mater. Energy Sustain.* 4 (2016) 10203–10211, <https://doi.org/10.1039/C6TA02788A>.
 - [20] W.J. Lee, P.S. Shinde, G.H. Go, C.H. Doh, Cathodic shift and improved photocurrent performance of cost-effective Fe_2O_3 photoanodes, *Int. J. Hydrog. Energy*. 39 (2014) 5575–5579, <https://doi.org/10.1016/j.ijhydene.2014.01.176>.
 - [21] Y. Kwon, A. Soon, H. Han, H. Lee, Shape effects of cuprous oxide particles on stability in water and photocatalytic water splitting, *J. Mater. Chem. A Mater. Energy Sustain.* 3 (2014) 156–162, <https://doi.org/10.1039/C4TA04863F>.
 - [22] S. Jamali, A. Moshaii, Improving photo-stability and charge transport properties of $\text{Cu}_2\text{O}/\text{CuO}$ for photo-electrochemical water splitting using alternate layers of WO_3 or CuWO_4 produced by the same route, *Appl. Surf. Sci.* 419 (2017) 269–276, <https://doi.org/10.1016/j.apsusc.2017.04.228>.
 - [23] P. Xu, J. Feng, T. Fang, X. Zhao, Z. Li, Z. Zou, Photoelectrochemical cell for unassisted overall solar water splitting using a BiVO_4 photoanode and Si nanorod photocathode, *RSC Adv.* 6 (2016) 9905–9910, <https://doi.org/10.1039/C5RA20115B>.
 - [24] J.H. Kim, Y.J. Jang, J.H. Kim, J.-W. Jang, S.H. Choi, J.S. Lee, Defective ZnFe_2O_4 nanorods with oxygen vacancy for photoelectrochemical water splitting, *Nanoscale* 7 (2015) 19144–19151, <https://doi.org/10.1039/C5NR05812K>.
 - [25] J.H. Kim, Y.J. Jang, S.H. Choi, B.J. Lee, J.H. Kim, Y.B. Park, C.-M. Nam, H.G. Kim, J.S. Lee, A multitude of modifications strategy of ZnFe_2O_4 nanorod photoanodes for enhanced photoelectrochemical water splitting activity, *J. Mater. Chem. A Mater. Energy Sustain.* 6 (2018) 12693–12700, <https://doi.org/10.1039/C8TA02161A>.
 - [26] S.S. Kalanur, J.-Y. Hwang, H. Seo, Facile fabrication of bitter-melon-shaped copper (II) tungstate thin films for improved photocatalytic water splitting, *J. Catal.* 350 (2017) 197–202, <https://doi.org/10.1016/j.jcat.2017.04.008>.
 - [27] I. Khan, A. Qurashi, Shape controlled synthesis of copper vanadate platelet nanostructures, their optical band edges, and solar-driven water splitting properties, *Sci. Rep.* 7 (2017) 14370, <https://doi.org/10.1038/s41598-017-14111-7>.
 - [28] L. Zhou, Q. Yan, A. Shinde, D. Guevarra, P.F. Newhouse, N. Becerra-Stasiewicz, S.M. Chatman, J.A. Haber, J.B. Neaton, J.M. Gregoire, High throughput discovery of solar fuels photoanodes in the $\text{CuO}-\text{V}_2\text{O}_5$ system, *Adv. Energy Mater.* 5 (2015) 1500968, <https://doi.org/10.1002/aenm.201500968>.
 - [29] P.F. Newhouse, D.A. Boyd, A. Shinde, D. Guevarra, L. Zhou, E. Soedarmadji, G. Li, J.B. Neaton, J.M. Gregoire, Solar fuel photoanodes prepared by inkjet printing of copper vanadates, *J. Mater. Chem. A Mater. Energy Sustain.* 4 (2016) 7483–7494, <https://doi.org/10.1039/C6TA01252C>.
 - [30] W. Guo, W.D. Chemelewski, O. Mabayoje, P. Xiao, Y. Zhang, C.B. Mullins, Synthesis and characterization of CuV_2O_6 and $\text{Cu}_2\text{V}_2\text{O}_7$: Two photoanode candidates for photoelectrochemical water oxidation, *J. Phys. Chem. C* 119 (2015) 27220–27227, <https://doi.org/10.1021/acs.jpcc.5b07219>.
 - [31] M. Kim, B. Joshi, H. Yoon, T.Y. Ohm, K. Kim, S.S. Al-Deyab, S.S. Yoon, Electrospun copper hexafluorovanadate (CuV_2O_6) and pyrovanadate ($\text{Cu}_2\text{V}_2\text{O}_7$) photoanodes for efficient solar water splitting, *J. Alloys. Compd.* 708 (2017) 444–450, <https://doi.org/10.1016/j.jallcom.2017.02.302>.
 - [32] C.-M. Jiang, G. Segev, L.H. Hess, G. Liu, G. Zaborski, F.M. Toma, J.K. Cooper, I.D. Sharp, Composition-dependent functionality of copper vanadate photoanodes, *ACS Appl. Mater. Interfaces* 10 (2018) 10627–10633, <https://doi.org/10.1021/acsami.8b02977>.
 - [33] C. Gadiyar, M. Strach, P. Schouwink, A. Loiudice, R. Buonsanti, Chemical transformations at the nanoscale: nanocrystal-seeded synthesis of $\beta\text{-Cu}_2\text{V}_2\text{O}_7$ with enhanced photoconversion efficiencies, *Chem. Sci.* 9 (2018) 5658–5665, <https://doi.org/10.1039/C8SC01314D>.
 - [34] J.A. Seabold, N.R. Neale, All First Row Transition Metal Oxide Photoanode for Water Splitting Based on $\text{Cu}_3\text{V}_2\text{O}_8$, (2015), <https://doi.org/10.1021/cm504327f>.
 - [35] C.-M. Jiang, M. Farmand, C.H. Wu, Y.-S. Liu, J. Guo, W.S. Drisdell, J.K. Cooper, I.D. Sharp, Electronic structure, optoelectronic properties, and photoelectrochemical characteristics of $\gamma\text{-Cu}_3\text{V}_2\text{O}_8$ thin films, *Chem. Mater.* 29 (2017) 3334–3345, <https://doi.org/10.1021/acs.chemmater.7b00807>.
 - [36] D. Cardenas-Morcoso, A. Peiro-Franch, I. Herraiz-Cardona, S. Gimenez, Chromium doped copper vanadate photoanodes for water splitting, *Catal. Today* 290 (2017) 65–72, <https://doi.org/10.1016/j.cattod.2016.11.002>.
 - [37] M.A. Lumley, K.-S. Choi, Investigation of pristine and (Mo, W)-doped $\text{Cu}_{11}\text{V}_6\text{O}_{26}$ for use as photoanodes for solar water splitting, *Chem. Mater.* 29 (2017) 9472–9479, <https://doi.org/10.1021/acs.chemmater.7b03587>.
 - [38] P.P. Sahoo, B. Zoellner, P.A. Maggard, Optical, electronic, and photoelectrochemical properties of the p-type $\text{Cu}_{3-x}\text{VO}_4$ semiconductor, *J. Mater. Chem. A Mater. Energy Sustain.* 3 (2015) 4501–4509, <https://doi.org/10.1039/C4TA04876H>.
 - [39] Y. Wang, L. Cao, J. Huang, J. Lu, B. Zhang, G. Hai, N. Jia, Enhanced cyclic performance of $\text{Cu}_2\text{V}_2\text{O}_7$ /reduced graphene oxide mesoporous microspheres assembled by nanoparticles as anode for Li-ion battery, *J. Alloys. Compd.* 724 (2017) 421–426, <https://doi.org/10.1016/j.jallcom.2017.07.070>.
 - [40] L. Pei, N. Lin, T. Wei, H. Liu, H. Yu, Formation of copper vanadate nanobelts and their electrochemical behaviors for the determination of ascorbic acid, *J. Mater. Chem. A Mater. Energy Sustain.* 3 (2015) 2690–2700, <https://doi.org/10.1039/C4TA05946H>.
 - [41] S. Meghana, P. Kabra, S. Chakraborty, N. Padmavathy, Understanding the pathway of antibacterial activity of copper oxide nanoparticles, *RSC Adv.* 5 (2015) 12293–12299, <https://doi.org/10.1039/C4RA12163E>.
 - [42] P. Wang, Y.H. Ng, R. Amal, Embedment of anodized p-type Cu_2O thin films with CuO nanowires for improvement in photoelectrochemical stability, *Nanoscale* 5 (2013) 2952–2958, <https://doi.org/10.1039/C3NR34012K>.
 - [43] L. Girardi, S. Shuang, G.A. Rizzi, A. Sartorel, C. Marega, Z. Zhang, G. Granozzi, Visible light driven photoanodes for water oxidation based on novel r-GO/ $\beta\text{-Cu}_2\text{V}_2\text{O}_7/\text{TiO}_2$ nanorods composites, *Nanomater. Basel Switz.* 8 (2018) 544, <https://doi.org/10.3390/nano8070544>.
 - [44] Y. Wang, Y. Lü, W. Zhan, Z. Xie, Q. Kuang, L. Zheng, Synthesis of porous $\text{Cu}_2\text{O}/\text{CuO}$ cages using Cu-based metal-organic frameworks as templates and their gas-sensing properties, *J. Mater. Chem. A Mater. Energy Sustain.* 3 (2015) 12796–12803, <https://doi.org/10.1039/C5TA01108F>.
 - [45] Q. Yu, W. Li, J. Liang, Z. Duan, Z. Hu, J. Liu, H. Chen, J. Chu, Oxygen pressure manipulations on the metal-insulator transition characteristics of highly (0 1 1)-oriented vanadium dioxide films grown by magnetron sputtering, *J. Phys. Appl. Phys.* 46 (2013) 055310, <https://doi.org/10.1088/0022-3727/46/5/055310>.
 - [46] Y. Matsumoto, M. Omai, I. Watanabe, E. Sato, Photoelectrochemical properties of the Zn-Ti-Fe spinel oxides, *J. Electrochem. Soc.* 133 (1986) 711–716, <https://doi.org/10.1149/1.2108660>.